Bulletin of the Seismological Society of America, Vol. 108, No. 3A, pp. 1369–1383, June 2018, doi: 10.1785/0120170195

Ⓔ

Constraints of Crustal Heterogeneity and Q(f) from Regional (< 4 Hz) Wave Propagation for the 2009 North Korea Nuclear Test

by Kim B. Olsen, Michael Begnaud, Scott Phillips, and Bo Holm Jacobsen

Abstract We carried out 3D finite-difference (FD) simulations (< 4 Hz) of regional wave propagation for the 2009 North Korea nuclear explosion and compared the synthetics with instrument-corrected records at stations INCN and TJN in South Korea. The source is an isotropic explosion with a moment magnitude of 4.1. Synthetics computed in the relatively smooth Sandia/Los Alamos National Laboratory SALSA3D (SAndia LoS Alamos 3D) velocity model significantly overpredict Rayleigh-wave amplitudes by more than an order of magnitude while underpredicting coda amplitudes. The addition to SALSA3D of a von Karman distribution of small-scale heterogeneities with correlation lengths of ~1000 m, a Hurst number of 0.1, and a horizontal-to-vertical anisotropy of ~5 produces synthetics in general agreement with the data. The best fits are obtained from models with a gradient in the strength of the velocity and density perturbations and strong scattering (10%) limited to the top 7.5–10 km of the crust. Deeper scattering tends to decrease the initial *P*-wave amplitudes to levels much below those for the data, a critical result for methods discriminating between explosive and earthquake sources. In particular, the amplitude at the onset of *Pn* can be affected by as little as 2% small-scale heterogeneity in the lower crust and upper mantle. Simulations including a constant Q of 200 (INCN) to 350 (TJN) below 1 Hz and a power-law Q(f) formulation at higher frequencies, with an exponent of 0.3, generate synthetics in best agreement with the data. In our simulations, very limited scattering contribution from the near-source area accumulates along the regional path.

Electronic Supplement: Description of the source time function used in the simulations, additional waveform comparisons (stations INCN and TJN), snapshots of wave propagation, and vertical cross sections and horizontal slices of the SAndia LoS Alamos 3D (SALSA3D) model with and without small-scale heterogeneities.

Introduction

The primary aim of nuclear-explosion monitoring is to be able to detect nuclear explosions, which includes discrimination between seismic records generated by different sources. The seismic signature in the records used in explosion monitoring is a combination of source, path, and local site effects. The origin of the source generally provides a constraint on the relative amount of *P*-, *S*-, and surface-wave phases included in the recorded waves. Although explosive sources typically give rise to records with a relatively large ratio of *P*-to-*S* waves, details of such trends depend on the length and character of the crustal path encountered by the waves.

In many cases, the closest available records are obtained from stations several hundred kilometers from the source, typically causing the addition of severe path effects to the recorded seismic waves. These path effects are generated by a combination of (frequency-dependent) anelastic attenuation, crustal scattering, focusing, and multipathing. Unless detailed modeling can be carried out to sufficiently high frequencies, path effects can lead to misinterpretation of the origin of the wavetrains. It is therefore imperative to be able to replicate the general characteristics of the seismic records from regional wave propagation.

Conventionally, regional modeling of crustal wave propagation has been carried out using either 1D or 2D approximations, due to the large computational cost associated with fully 3D deterministic models. However, recent advances in available supercomputing resources have facilitated full-waveform simulations in 3D velocity models for

frequencies up to several hertz. For example, Takemura *et al.* (2015) simulated wave propagation out to distances of about 70 km from explosive and earthquake sources for frequencies up to 4.2 Hz in Japan. Rodgers *et al.* (2010) investigated topographic scattering effects, and Pitarka *et al.* (2015) simulated the seismic signature of a chemical explosion in 3D crustal models using finite-difference (FD) methods. Wang *et al.* (2016) showed that including topographic scattering can improve the accuracy of source location.

Accurate ground modeling motion requires that anleastic attenuation, typically parameterized by Q, be included. For frequencies less than about 1 Hz, a frequency-independent Q approach has generally been sufficient to fit the distance decay of seismic amplitudes caused by anelastic losses (e.g., Olsen, 2000; Cui *et al.*, 2010; and many other studies). However, as frequencies increase, seismic data demands frequency dependency of Q, with progressively decreasing attenuation (e.g., Raoof *et al.*, 1999; Lekic *et al.*, 2009; McNamara *et al.*, 2012; Phillips *et al.*, 2014). Such frequency dependency of Q can be formulated numerically for deterministic ground-motion simulations (Withers *et al.*, 2015). Moreover, as frequencies grow, small-scale heterogeneities of the medium increasingly affect the wave propagation via scattering. Although not feasible for directly mapping the *in situ* small-scale crustal variation, the velocity and density perturbations can be formulated statistically. Using such techniques, several studies have proposed ranges of the controlling parameters from analyses of sonic logs and V_{S30} data (e.g., Savran and Olsen, 2016) and ambient noise modeling (Nakata and Beroza, 2015).

The primary objective of this study is to push the simulation of wave propagation in state-of-the-art 3D crustal models from shallow explosive sources to larger distances and higher frequencies, using validation from broadband seismic data. We have reached a point at which high-performance computing capabilities and sophistication of scientific models allow simulating high-frequency (here, up to 4 Hz) regional wave propagation to distances of several hundred kilometers. Our approach includes a highly scalable FD method, a 3D crustal structure, $Q(f)$, and statistical descriptions of small-scale velocity and density perturbations. First, we describe the velocity and $Q(f)$ models used in the wave propagation. Then, the source and associated parameters used for the 2009 North Korea nuclear test are described, followed by a description of the seismic data used to constrain the model parameters at stations INCN and TJN in South Korea. We show ground-motion synthetics compared with data at the two stations in the SALSA3D (SAndia LoS Alamos 3D, Ballard *et al.*, 2016) model, with and without various distributions of small-scale heterogeneities, exploring their depth dependency, strength, horizontal-to-vertical anisotropy, and proximity to the source. Because our focus in this study is on the continental path, we highlight the results for station INCN in the main article and leave the results at TJN, where waves from the source propagate partly in the offshore region, for the Ⓔ electronic supplement available to this article.

Numerical Modeling

We used the AWP-ODC-GPU code to simulate all wave propagation presented in this study. AWP-ODC-GPU is a highly scalable graphic processing unit (GPU)-based anelastic wave propagation code that solves the 3D velocity-stress wave equation explicitly by a staggered-grid FD method with fourth-order accuracy in space and second-order accuracy in time (Olsen, 1994; Cui *et al.*, 2013). The code has been extensively validated for a wide range of problems in 3D crustal models (e.g., Day *et al.*, 2008; Bielak *et al.*, 2010).

Anelastic attenuation plays an important role for the regional propagation distances considered here. A power-law description of the form $Q = Q_0(f/f_0)^\gamma$ has been successfully used to model Q in broadband simulations, in which Q_0 and γ are region-specific parameters. Here, we use the accurate coarse-grain memory-variable approach implemented in AWP-ODC by Withers *et al.* (2015), with separate values of Q for *P* waves (Q_P) and *S* waves (Q_S) specified for each grid point in the model.

Velocity Model

We used velocity information from the SALSA3D global 3D tomography model of the Earth's crust and mantle. The model was developed to obtain improved locations of explosive sources, with *P*- and *S*-wave velocity distributions obtained by separate tomographic inversions. Density in our calculations was calculated from V_S using the relation by Nafe and Drake (1960) for $V_P < 6.2$ km/s and Birch's law (Birch, 1961) for $V_P > 6.2$, with a smooth transition between the two regions.

Figure 1 shows the distribution of V_S at a depth of 3.3 km in the region used to model wave propagation from the North Korea nuclear test site (NKNTS), a 450 km (east–west) by 670 km (north–south [N-S]) by 80 km (depth) subvolume of the SALSA3D model at a uniform grid spacing of 100 m everywhere (24 billion grid points). The SALSA3D model was produced as a triangular tessellation with minimum grid spacing of 1° (for areas with dense ray coverage), combining the National Nuclear Security Administration Unified Model for Eurasia (Pasyanos *et al.*, 2004; Steck *et al.*, 2004) and the CRUST 2.0 model (see Laske and Masters, 1997). Note the higher velocities inside the N-S-oriented band within the Korean peninsula, as compared to the continental shelf to the east. It is clear that SALSA3D in our area of interest is considerably smooth, with apparent horizontal correlation lengths on the order of tens to hundreds of kilometers. This lack of smaller scale variation is addressed separately through a statistical approach, in order to introduce realistic scattering for frequencies up to 4 Hz (see the Small-scale Media Heterogeneities section). In the Discussion section, we test the effects of larger scale (blocky) variation in the crust.

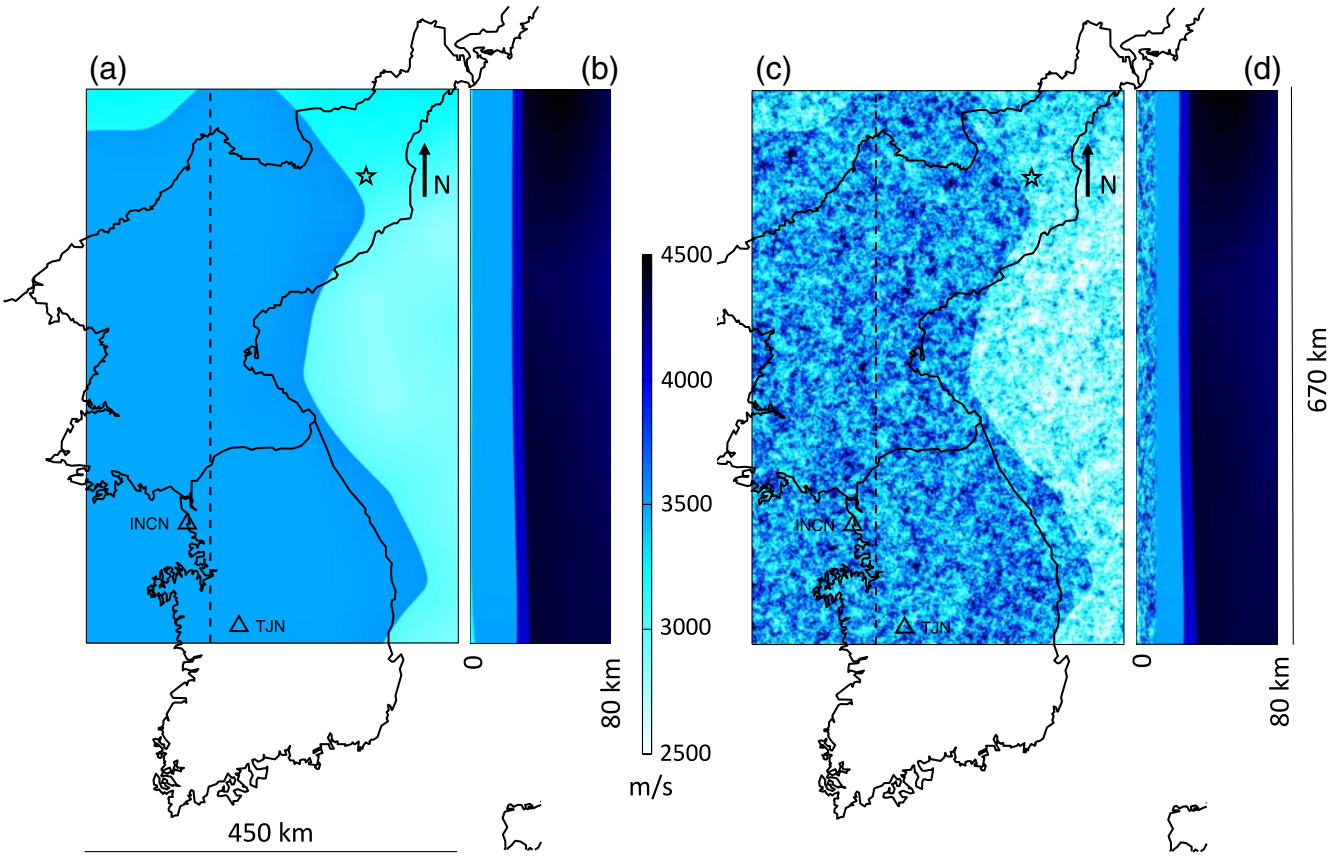

Figure 1. *S*-wave velocity from the SAndia LoS Alamos 3D (SALSA3D) model at 3.3 km depth (a) without and (c) with a distribution of small-scale heterogeneities ($a = 1000$ m, $\upsilon = 0.1$, $\sigma = 10\%$, H/V = 5, model 6 in Table 1). (b,d) Cross sections along the north–south (N-S) profile denoted by the dashed white line are shown next to the depth sections. The star denotes the source location for the 25 May 2009 North Korea nuclear test. Two stations (INCN and TJN) in South Korea have instrument-corrected records available (white triangles). The color version of this figure is available only in the electronic edition.

Source Description

We modeled the source for the 2009 NKNTS at 41.2914° N, 129.0819° E, at a depth of 600 m below the surface, consistent with the location found by Patton and Pabian (2014). Ford *et al.* (2009) and Shin *et al.* (2010) estimated a total M_w for the event of ~4.5. However, Ford *et al.* (2009) also found that the isotropic component of the source provided fits to the data almost as well as the full solution. In our model, the source is therefore defined as an isotropic, purely explosive point source with a moment magnitude of 4.1 (moment 1.58×10^{15} N·m), based on the results by Ford *et al.* (2009) and Shin *et al.* (2010). Ⓔ Figure S1 shows details of the simulated source function.

Seismic Data Constraints

We use instrument-response corrected ground-motion histories from stations INCN and TJN (see Fig. 1 for station locations). Data from additional stations in South Korea exist (see, e.g., Shin *et al.*, 2010) but were not accessible for our study. The data were low-pass filtered to 4 Hz with a 10-pole Butterworth filter with two forward passes, and the horizontal components were rotated into radial and transverse components. For the waveform comparisons presented in this study, we repeated this processing procedure for the synthetics.

Regional Wave Propagation

Several studies have reported values for Q in east Asia, associated with specific phases such as *Pn*, *Pg*, *Sn*, and *Lg* waves, including Mitchell *et al.* (1997), Xie *et al.* (2006), Hong and Rhie (2009), and Ford *et al.* (2010). These studies typically report crustal-wide values of Q_0 and γ, assuming a power-law relation $Q = Q_0(f/f_0)^\gamma$, obtained from attenuation tomography methods. In general, these results tend to agree reasonably well for the Korean Peninsula. While these studies typically report Q values associated with phases such as *Pn*, *Pg*, *Sn*, and *Lg*, it is not immediately clear how these Q values relate to those for *P* and *S* waves, which are required for the viscoelastic modeling with AWP-ODC. As a starting point for our modeling, we select values of $Q_{os} = Q_{op} = 350$ and $\gamma = 0.3$ ($f_0 = 1$ Hz) as a reference model for

Table 1
Q(f) and Small-Scale Heterogeneity Parameters for Finite-Difference (FD) Models

Model	a (m)	R (km)	σ (%) $d < d_1$	d_1 (km)	σ (%) $d > d_2$	d_2 (km)	H/V	Seed	Q_0	γ
1	—	—	—	—	—	—	—	—	350	0.3
2	1000	5	5	—	5	—	5	1	350	0.3
3	1000	5	10	—	10	—	5	1	350	0.3
4	150	5	10	—	10	—	5	1	350	0.3
5	1000	5	10	—	10	—	5	1	200	0.3
6	1000	5	10	10	2	12.5	5	1	200	0.3
6a	1000	0	10	10	0	12.5	5	1	200	0.3
6b	1000	0	10	10	2	12.5	5	1	300	0.3
6c	1000	0	10	10	2	12.5	5	1	400	0.3
6d	1000	0	10	10	2	12.5	5	1	500	0.3
7	1000	0	10	7.5	2	10	5	1	200	0.3
7a	1000	0	10	7.5	0	10	5	1	200	0.3
7b	1000	0	10	7.5	0	10	5	2	200	0.3
7c	1000	0	10	7.5	0	10	5	4	200	0.3
7d	1000	0	10	7.5	0	10	5	5	200	0.3
7e	1000	0	10	7.5	0	10	5	6	200	0.3
8	1000	5	10	5	2	5	5	1	200	0.3
9	1000	5	10	2.5	2	2.5	5	1	200	0.3
10	1000	5	10	10	2	12.5	1	1	200	0.3
11	1000	5	10	10	2	12.5	7	1	200	0.3
12	1000	5	10	10	2	12.5	10	1	200	0.3
13	150	0	10	10	0	12.5	5	1	200	0.3
14	2000	0	10	10	0	12.5	5	1	200	0.3
15	3000	0	10	10	0	12.5	5	1	200	0.3
16	1000	0.5	10	10	0	12.5	5	1	200	0.3
17	1000	0.5	10	10	0	12.5	5	2	200	0.3
18	1000	0.5	10	10	0	12.5	5	4	200	0.3
19	1000	0.5	10	10	0	12.5	5	5	200	0.3
20	1000	0.5	10	10	0	12.5	5	6	200	0.3
21	5000	0	10	7.5	0	10.0	20	1	200	0.3

All models use $\nu = 0.1$.

our simulations (model 1, Table 1), based on the published studies listed above.

Figure 2 shows three-component snapshots of velocity wave propagation in model 1. The snapshots show coherent *P* and surface waves developing at the NKNTS at 27.5 s, with some limited *P*–*S* scattered energy emerging inbetween. At 82.5 s, the amplitudes of the *P* waves have diminished to a level not observable relative to that for the coherent surface waves at 82.5 s and later times. The surface waves impinge on South Korea around 137.5 s and propagate between stations INCN and TJN at 192.5 s. The largest surface-wave amplitudes are found on the vertical component, consistent with the particle motion of a Rayleigh wave. The surface waves are slowed down in the offshore area east of the Korean Peninsula due to lower seismic velocities.

Comparisons of observed and simulated 0–4 Hz waveforms in the SALSA3D model for the 2009 NKNTS at INCN and TJN are shown in Figure 3 and Ⓔ Figure S3, respectively. In these figures, and subsequent waveform comparisons, we identify the expected arrival times for *Pn* as 7.0 s+ dist/$vg(Pn)$, *Pg* as dist/$vg(Pg)$, *Sn* as 12.0 s + dist/$vg(Sn)$, and *Lg* as dist/$vg(Lg)$, in which dist is the horizontal distance between the source and station, and vg is the group velocity of the particular phase. We use group velocity ranges of 7.6–8.2 km/s for *Pn*, 5.2–6.2 km/s for *Pg*, 4.0–4.7 km/s for *Sn*, and 3.0–3.6 km/s for *Lg* to define windows for the phases.

The radial and vertical components show large-amplitude initial *Pn* and *Pg* waves and a strongly dispersive Rayleigh wave starting at the end of the *Lg* window, persisting ~25 s past the window. The transverse component has little initial *S*-wave energy, but a dispersive Love wave appears simultaneously with the Rayleigh wave. It is evident from the comparison that the reference model very poorly reproduces the data from the two stations, in both time and frequency domains. Specifically, we observe the following areas in need of improvement: (1) although initial (*P*) phases in the synthetics arrive approximately at the expected time, their peak amplitudes are too large; (2) the surface waves are too energetic and arrive too late; (3) the amplitudes between the *P* wave and surface waves are too small; and (4) the spectral amplitudes are overpredicted for frequencies higher than about 0.4 Hz.

The details of the misfits in Figure 3 and Ⓔ Figure S3 suggest that our reference model is deficient in scattering by features with smaller length scales, not included in the rather smooth SALSA3D model. Scattering by geological features

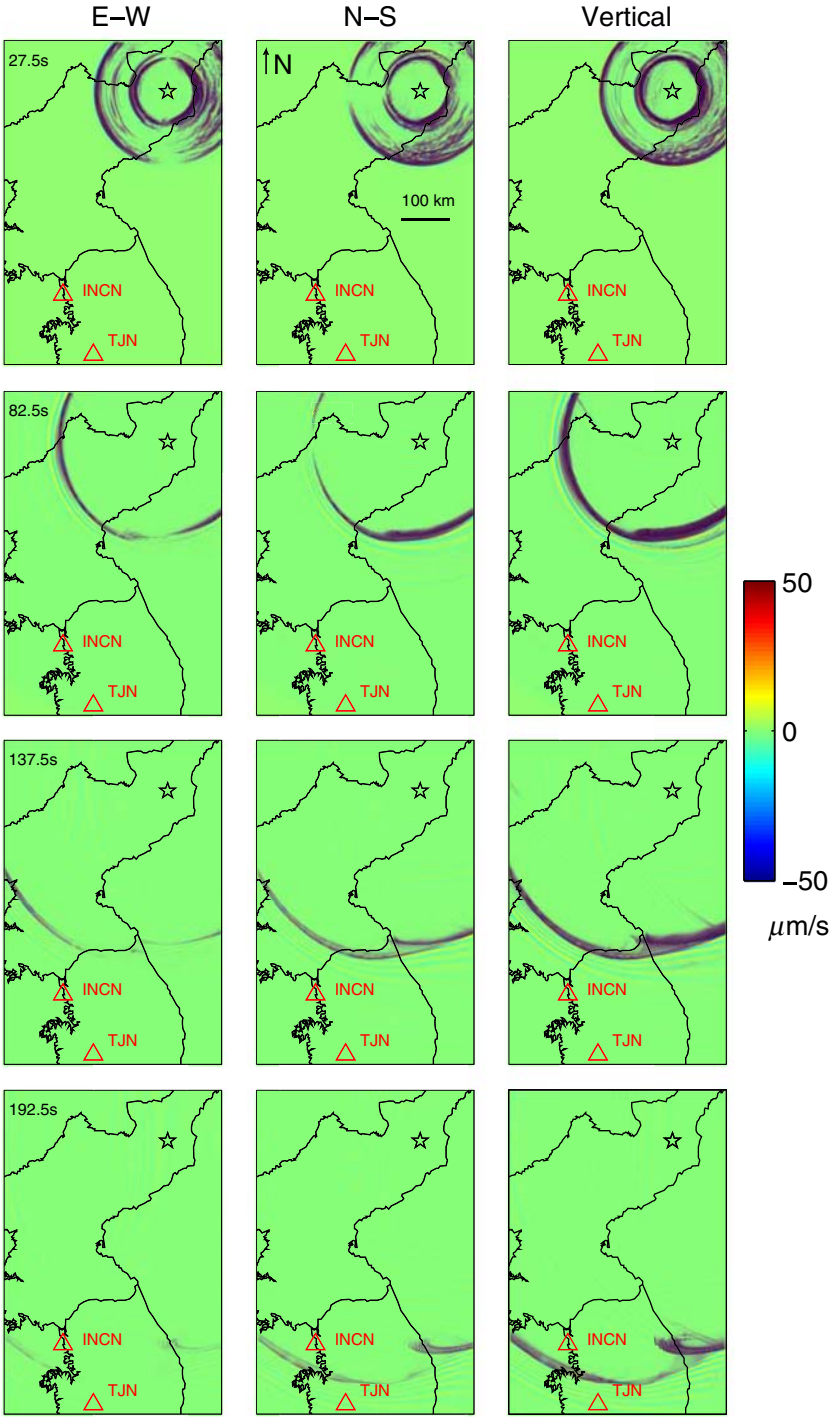

Figure 2. Snapshots of wave propagation (< 4 Hz) in SALSA3D (model 1, Table 1). The color version of this figure is available only in the electronic edition.

with scale lengths less than ~10 km, insufficiently represented in the model, is expected to introduce incoherency in and therefore decrease the amplitude of the *P* and surface waves, as well as generate converted body waves between the *P*- and surface-wave arrivals and increase the late coda wavetrain. To improve the waveform fits, we will introduce small-scale scattering in the SALSA3D model using a statistical approach.

Small-Scale Media Heterogeneities

Statistical Description. Small-scale heterogeneities can be described statistically, for example, using von Karman spatial correlation functions shown in equation (1) with Fourier transform in equation (2) as follows:

$$\Phi_{\upsilon,L}(r) = \sigma^2 \frac{2^{1-\upsilon}}{\Gamma(\upsilon)} \left(\frac{r}{a}\right)^{\upsilon} K_{\upsilon}\left(\frac{r}{a}\right) \quad (1)$$

$$P(k) = \frac{\sigma^2 (2\sqrt{\pi}a)^E \Gamma(\upsilon + E/2)}{\Gamma(\upsilon)(1 + k^2 a^2)^{\upsilon + E/2}} \quad (2)$$

(Tatarski, 1961), or using other statistical descriptions (e.g., Gaussian or Exponential correlation functions, see e.g., Frankel and Clayton, 1986). Here, K_υ is the modified Bessel function of order υ (Hurst exponent), Γ is the Gamma function, a is the correlation length, and σ is the standard deviation. Constraints on a, ν, and σ can be obtained from sonic logs, digitized geological maps, and V_{S30} measurements (e.g., Holliger and Levander, 1992; De *et al.*, 1994; Levander *et al.*, 1994; Wu *et al.*, 1994; Holliger, 1996, 1997; Dolan *et al.*, 1998; Plesch *et al.*, 2014; Nakata and Beroza, 2015; Savran and Olsen, 2016). These studies report Hurst exponents of 0.0–0.3 and correlation lengths between 60 and 160 m in the vertical direction, and horizontal-to-vertical (H/V) anisotropy between ~2 and 25. There is considerable variation in the correlation lengths found among the studies, reflecting the variable constraints from the underlying data (e.g., teleseismics may favor longer correlation lengths as compared to data from near-field stations). Moreover, the results from analysis of detailed sonic logs with sample spacings < 1 m are prone to producing smaller (high-frequency) values than those from much more coarsely distributed measurements (such as V_{S30}).

Other constraints on the parameters of the small-scale heterogeneities are obtained from applying the statistical distributions in wave propagation simulations. For example, Frankel and Clayton (1986) used three distinct spatial correlation functions: self-similar (corresponding to a $\nu = 0.0$), exponential (corresponding to $\nu = 0.5$), and Gaussian. By testing end-member cases of the von Karman correlation functions, their 2D simulations provided

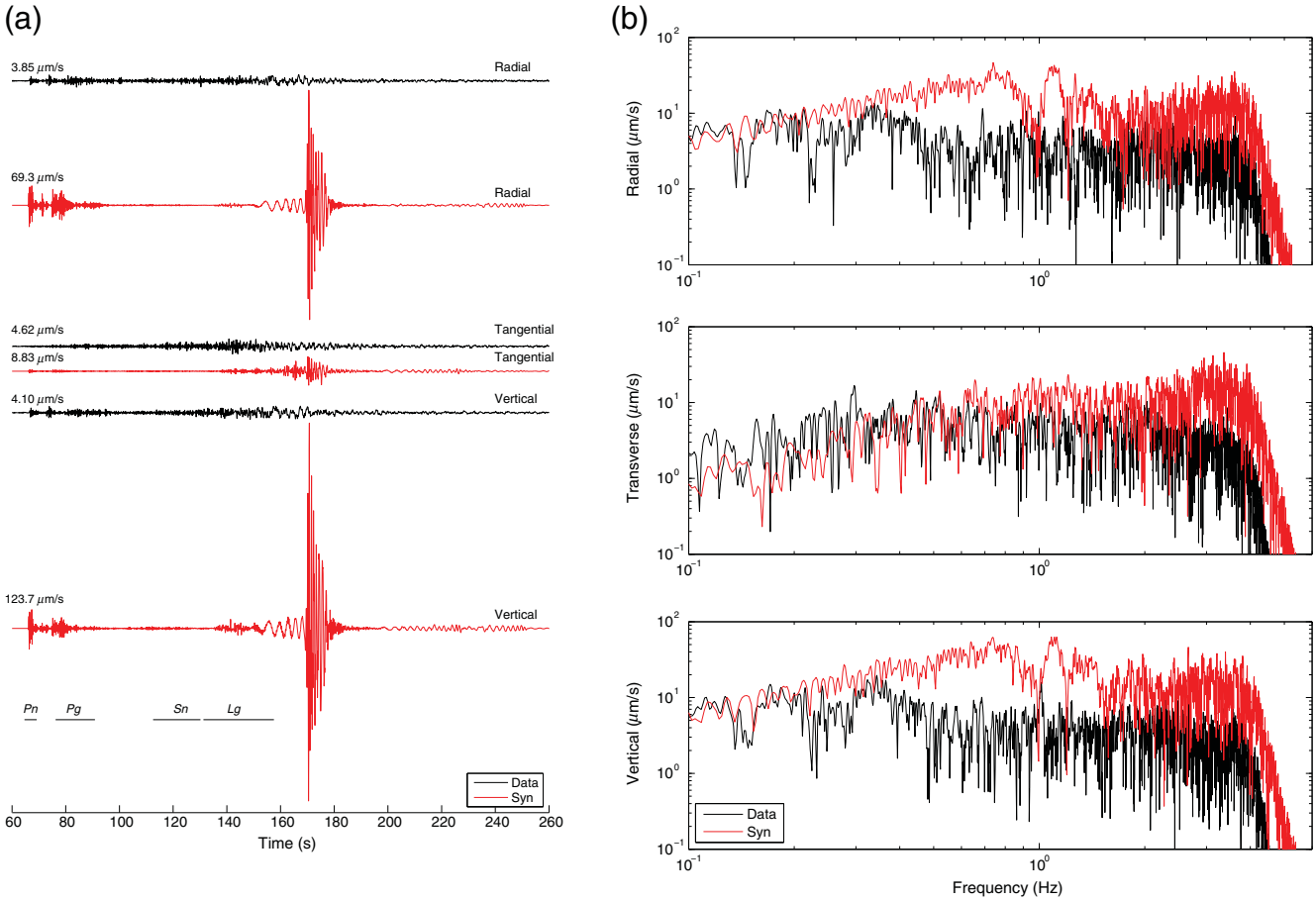

Figure 3. Comparison of observed and synthetic waveforms at INCN for the SALSA3D model with small-scale heterogeneity model 1 (Table 1) in (a) time and (b) frequency domains. The color version of this figure is available only in the electronic edition.

constraints on ν estimates for the small-scale heterogeneities that fall in the range [0.0, 0.5] (preferred value of 0.0). Wagner and Langston (1992) and Wagner (1996) provided guidance on the relative scattering effects from variation in ν, a_z, a_x/a_z, and σ, using 2D FD simulations with plane wave and point sources, respectively. Hartzell *et al.* (2010) used $\nu = 0.0$ with $a = 5$–10 km and $\sigma = 5\%$–10%, whereas Olsen and Jacobsen (2011) included statistical distributions with ν values of -0.5, 0, and 0.5, $a = 250$ m and $\sigma = 5\%$–10% in their simulations. Imperatori and Mai (2013) used $\nu = 0.3$ and a ranging from hundreds of meters to kilometers.

We computed distributions of small-scale heterogeneities by spectral coloring of Gaussian random numbers using equation (2) with parameters based on the published studies discussed earlier, and the velocity and density perturbations were added to the SALSA3D model. Figure 1 (right) shows horizontal and vertical slices of V_S, in which $a = 1000$ m, $\nu = 0.1$, $\sigma = 10\%$, $\mathrm{H/V} = 5$ (model 2, Table 1). In the following, we use trial-and-error modeling to constrain the statistical parameters of the von Karman and anelastic parameters generating synthetics with the best fit to data. In the series of tests concerning a particular parameter, all other parameters are kept constant.

Scattering Effects from Depth-Independent Models. Figure 4 (INCN) and Ⓔ Figure S4 (TJN) show a comparison of data and simulations including a von Karman model with models 2–5 (see Table 1). The small-scale heterogeneities are added to the entire depth extent of the reference model, and we use $\gamma = 0.3$ for the frequency-dependent power-law exponent. Compared with model 1 without small-scale heterogeneities, model 2 with $\sigma = 5\%$ and $Q_0 = 350$ still produces a coherent Rayleigh wave, albeit with reduced amplitude, and the amplitudes between the P and surface waves and the coda following the surface waves continue to be larger than that for the data. When σ is increased to 10% throughout the model (model 3), the surface-wave amplitudes are further reduced, the amplitudes between the P and surface waves are now similar to or smaller than those for the data, and the coda amplitude after the surface waves is increased from the 5% case (model 2). Model 3 generates synthetics with coda amplitudes similar to data at TJN, but tends to overpredict those at INCN.

The Hurst number of the small-scale heterogeneities in models 2–5 ($\nu = 0.1$) was selected in agreement with the variogram analysis of borehole sonic logs from the Los Angeles basin (Savran and Olsen, 2016). This analysis also found vertical correlation lengths of 50–150 m, much shorter than

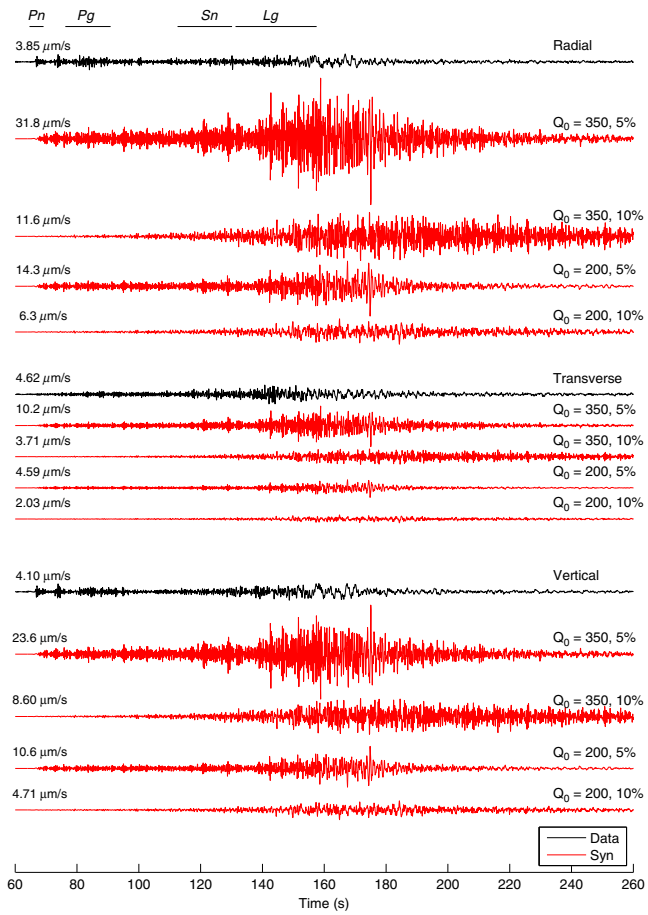

Figure 4. Comparison of observed and synthetic waveforms at INCN for the SALSA3D model with models 2–5 (Table 1). The color version of this figure is available only in the electronic edition.

the $a = 1000$ m used in models 2 and 3. However, it is clear from model 4, using $a = 150$ m and $\sigma = 10\%$, that the shorter correlation length, while reducing the higher frequency amplitudes in the synthetics, still produces Rayleigh-wave amplitudes much larger than those in the data. Thus, varying the parameters of the small-scale heterogeneities does not appear to produce a satisfactory fit of the synthetics to the data. Instead, a lower Q_0 of 200 with $a = 1000$ m and $\sigma = 10\%$ (model 5) produces synthetics with a closer match to the data at INCN but generally underpredicts the data at TJN. This result suggests that the path from the NKNTS to TJN is characterized by somewhat smaller low-frequency attenuation ($Q_0 \sim 350$) than that to INCN ($Q_0 \sim 200$).

Probably the most pronounced effect of models 2–5 on the synthetics is the reduction of the *Pn* amplitude to values much below those for the data. We examine in the following section whether this issue can be overcome using a depth dependency of σ.

Scattering Effects from Depth-Dependent Models. In agreement with the increase in lithostatic pressure and ductility of crustal material at deeper depths, the strength of the small-scale heterogeneities may decrease as well. To test such depth dependency of the scattering, we simulated wave propagation in four different gradient models of von Karman statistical distributions of small-scale heterogeneities (Fig. 5, INCN, and Ⓔ Fig. S5, TJN; models 6–9 in Table 1). The gradient models are all characterized by $\sigma = 10\%$ from the surface to a depth of d_1 (km), $\sigma = 2\%$ below a depth of d_2 (km), and a linear gradient in between. The values of d_1 and d_2 are listed by the synthetics. Here, we choose to use the relation $Q(f) = 200f^{0.3}$, which produced an optimal fit for INCN using model 5.

It is clear from Figure 5 and Ⓔ Figure S5 that the decrease in strength of the small-scale heterogeneities with depth in the upper crust improves the fit between the data and synthetics by generating larger-amplitude initial P waves and by improving the amplitude of converted phases between the *P* and surface arrivals. Models 6 and 7 are selected for further analysis in the following sections based on their favorable fit to the data.

The scattering originating from the deeper parts of the model is further illustrated in Figure 6 (INCN) and Ⓔ Figure S6 (TJN), in which the effects of the scattering from models with $\sigma = 0\%$ and 2% below the lower threshold depth (d_2) in the gradient models of Figure 5 and Ⓔ Figure S5 are highlighted. The results show that even a small σ value of 2% below d_2 can have a significant effect on the wavetrain, including the first-arriving *P* phases. Specifically, the gradient model with $\sigma = 2\%$ generates a gradual onset of *Pn* over 1–2 s, affecting the initial amplitude. On the other hand, if small-scale heterogeneities are omitted below d_2, the arrival time and amplitude of the *Pn* amplitudes are more impulsive. This result can have implications for techniques discriminating between explosive and earthquake sources, based on ratios of *P*- and *S*-wave amplitudes. The modeling effects of the small-scale heterogeneities thus suggest that the strength of scattering in the Earth's lower crust and the upper mantle strongly controls the amplitude and character of the initial *P* waves.

Constraints on Anisotropy of the Small-Scale Crustal and Mantle Heterogeneities. Several studies estimated the H/V anisotropy of the small-scale heterogeneities in the crust from statistical analyses (e.g., Plesch *et al.*, 2014, from a set of closely spaced boreholes in the Los Angeles basin, California, estimating H/V ~ 25; Nakata and Beroza, 2015, using random-field model representations of a 3D *P*-wave velocity model at Long Beach, California, finding H/V ~ 5). Whereas these H/V measurements are based on analysis of representations of the crustal structure, we here constrain the statistical anisotropy from modeling regional wave propagation from the NKNTS to stations INCN and TJN. Figure 7 (INCN) and Ⓔ Figure S7 (TJN) show waveform comparisons for the gradient model of small-scale heterogeneities with $\sigma = 10\%$ from the surface to a depth of 10 km, $\sigma = 2\%$ below a depth of 12.5 km, with H/V = 1, 5, 7, and 10 (models 6, and 10–12, Table 1). The model with no

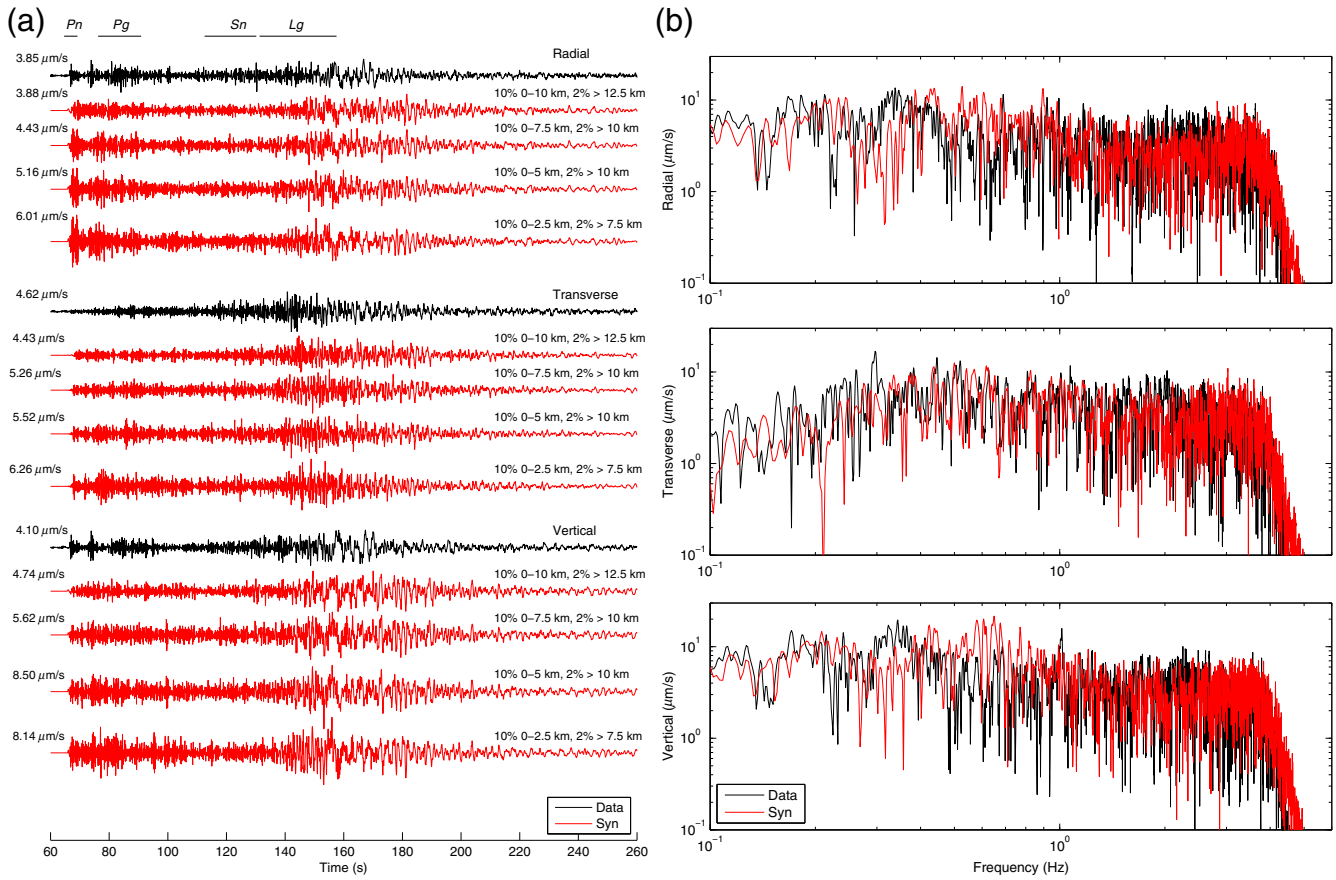

Figure 5. (a) Comparison of observed and synthetic waveforms at INCN for models 6–9 (Table 1). The gradient models are all characterized by $\sigma = 10\%$ from the surface to a depth of d_1 km, $\sigma = 2\%$ below a depth of d_2 km, and a linear gradient in between. The values of d_1 and d_2 are listed by the synthetics. (b) Comparison in the frequency domain for model 6 (Table 1). The color version of this figure is available only in the electronic edition.

anisotropy (H/V = 1) generates a Rayleigh-wave deficiency in higher frequencies and amplitude larger than that observed in the data. The Rayleigh wave for H/V values of 7 and 10, while limited to a narrower time window, also overpredicts the amplitude of the phase in the data. The (high-frequency) energy associated with the *Pn* phases for the simulations with H/V = 1, 7, and 10 are larger than that for the data. The value of H/V that generates the synthetics in best agreement with data for both initial *P* and surface waves, is 5, in agreement with the results by Nakata and Beroza (2015).

Constraints on Correlation Length of the Small-Scale Crustal and Mantle Heterogeneities. Previous modeling studies that have included statistical models of small-scale heterogeneities have considered a tremendous range of correlation lengths for the velocity perturbations, from tens of meters to 10 km. Here, we test whether an optimal value for the correlation length of the crust and mantle between NKNTS and stations INCN and TJN can be found, in terms of the match between data and synthetics at the two stations. Figure 8 and Ⓔ Figure S8 show the waveform fits at INCN and TJN, respectively, for Q(f), ν, and σ of model 6 and correlation length of 150, 1000, 2000, and 3000 m (models 13, 6, 14, and 15, Table 1). The synthetics for $a = 150$, 2000, and 3000 m tend to generate large-amplitude Rayleigh waves (~160–180 s at INCN, ~200–230 s at TJN), with similarity to those obtained in model 1 without small-scale heterogeneities (Fig. 3). On the other hand, the synthetics obtained from the model with $a = 1000$ m (model 6) generally resembles the waveform characteristics of the data, with much smaller Rayleigh-wave amplitudes, as compared to those from the models with shorter and longer values of a. Based on this result, we adopt a value of 1000 m as an average correlation length for the path between the NKNTS and the western North Korean Peninsula.

Near-Source Scattering and Generation of S*-Wave Energy.* An explosive source with limited tectonic release and other near-source effects primarily generates compressional seismic energy (e.g., Ford *et al.*, 2009; Shin *et al.*, 2010). However, records from explosive sources at regional distances often contain considerable *S*-wave energy (as is the case for the observed transverse component at INCN and TJN in our models). Our simulations show that crustal

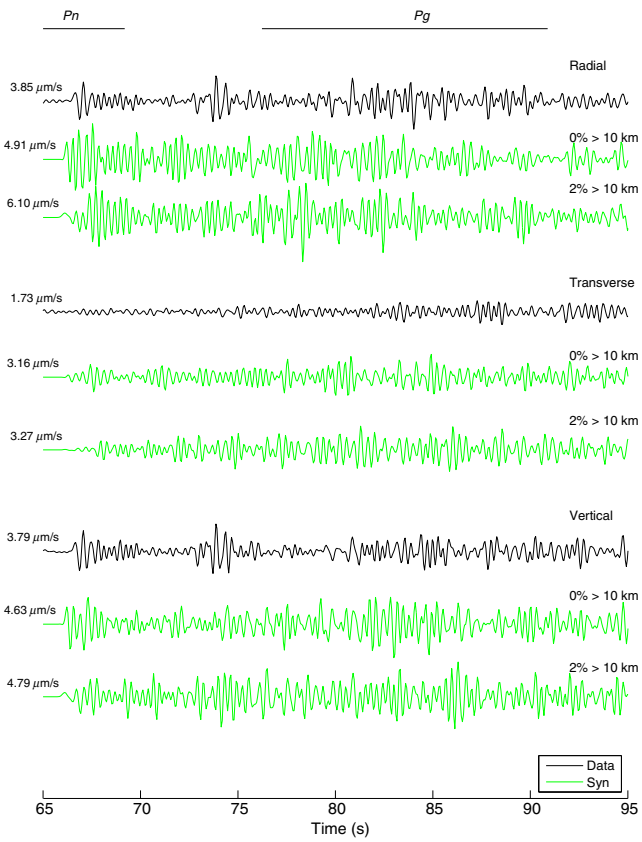

Figure 6. Enlarged view of the time domain comparison for INCN using models 7 and 7a (Table 1). Peak velocities listed refer to the time interval shown. The color version of this figure is available only in the electronic edition.

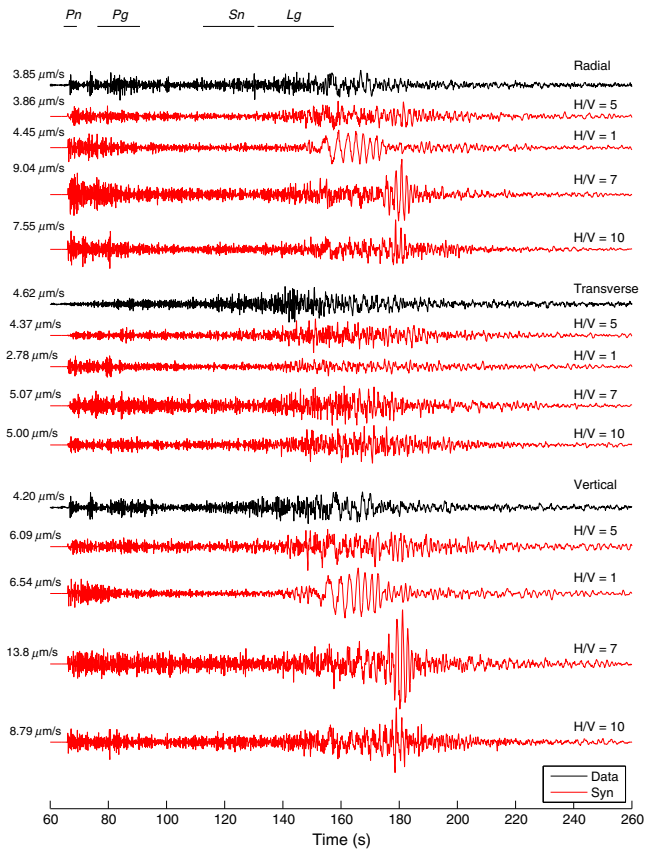

Figure 7. Comparison at INCN of the scattering effects from anisotropy in the small-scale heterogeneities, quantified by the ratio of horizontal-to-vertical (H/V) dimensions of the velocity and density perturbations. Results for H/V = 1, 5, 7, and 10 (models 10, 6, 11, and 12, Table 1) are shown. The color version of this figure is available only in the electronic edition.

and mantle scattering processes from small-scale heterogeneities can explain a large part of the *S*-wave and Love-wave energy on the transverse components recorded at INCN and TJN.

The FD modeling technique allows us to investigate which fraction of the *S*-wave energy is generated in the near-source region in the simulations. Toward this goal, Figure 9 (INCN) and Ⓔ Figure S9 (TJN) compare synthetics with small-scale heterogeneities added along the gradient from model 6 (Table 1), in which the small-scale heterogeneities are omitted within a spherical volume with radii of 0, 1, 5, and 10 km. At first glance, the synthetics for the four different models are very similar, in both amplitude and general characteristics of the phases. The synthetics for the model with $R = 0$ km are visually almost identical to those with $R = 1$ and 5 km, while smaller variations in phase and a slight decrease in peak amplitude start to appear in the synthetics for $R = 10$. These results apply to all three components, including the transverse component, where the contribution from an isotropic source is expected to be minimal. Thus, Figure 9 and Ⓔ Figure S9 show that scattering within a narrow region around the source contributes negligibly to the *S*-wave energy simulated at INCN and TJN.

Figure 10 shows snapshots of velocity wave propagation in model 6 (Table 1). The contrast of the wavefield in Figure 10 compared with that in Figure 3 is striking, primarily due to the amount of crustal scattering generated by the small-scale heterogeneities. At 27.5 s, *P*-to-*S* and *P*-to-*P* scattering dominates the area between the *P* and surface waves. The surface waves, characterized by large-amplitude coherent wavetrains in the model without small-scale heterogeneities (Fig. 3), appear as a 100+ km-wide band of scattered energy at 82.5 s at which amplitudes diminish away from a central high. At later times (82.5 and 137.5 s), the largest scattered surface waves occur offshore east of the Korean Peninsula in the lower velocity material.

Variation of Q_0 from NKNTS to INCN and TJN

Comparison of Figure 4 and Ⓔ Figure S4 suggested that the average Q_0 values between NKNTS and INCN may be smaller than that between NTNTS and TJN, inferred from the fit between data and synthetics computed with no depth dependency in the simulations. Figure 11 (INCN) and Ⓔ Figure S10 (TJN) confirm this difference, showing the

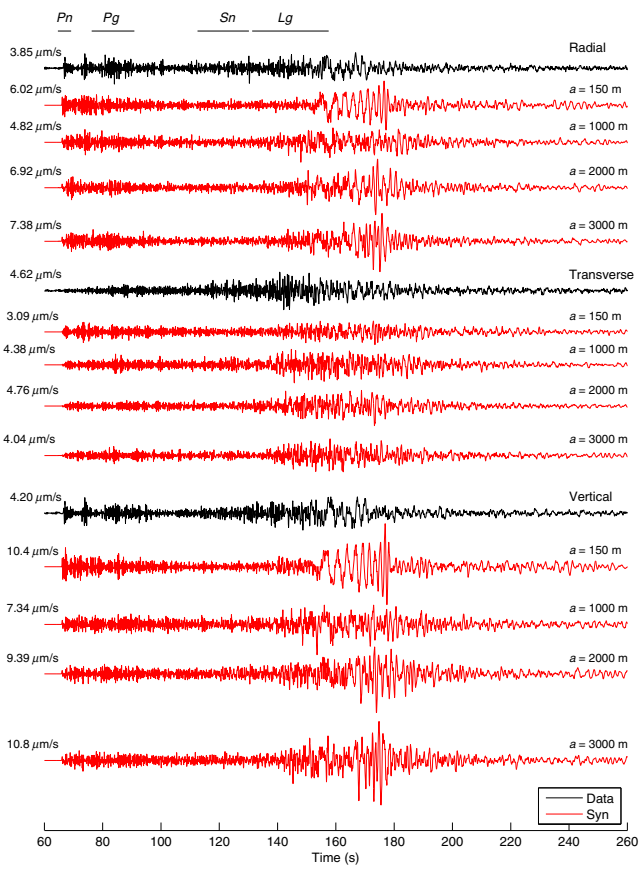

Figure 8. Comparison at INCN of the scattering effects from different correlation length in the distribution of small-scale heterogeneities (150, 1000, 2000, and 3000 m) as defined by models 13, 6a, 14, and 15 (Table 1). The color version of this figure is available only in the electronic edition.

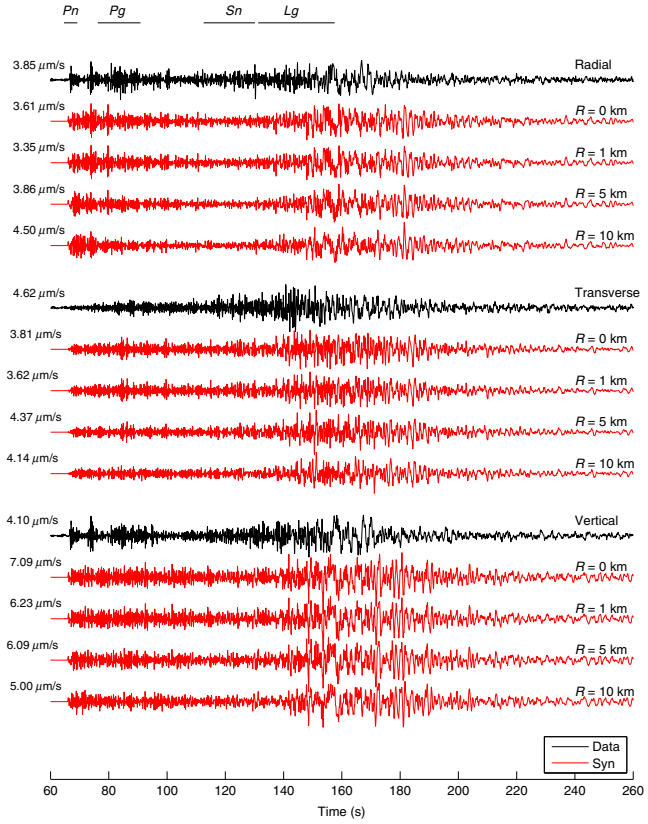

Figure 9. Significance of near-source scattering effects from small-scale heterogeneities at INCN. The statistical model (model 6, Table 1) has been removed within radii (R) of 0–10 km from the source, listed by the synthetics. The color version of this figure is available only in the electronic edition.

variation in waveforms at the two stations for the parameters of models 6 and 6b–d (Table 1), showing the effect of Q_0 values between 200 and 500. The variation of the peak amplitudes of more than a factor of 3 across the models shows a strong sensitivity to and promise for resolving Q_0 in the simulations. Although $Q_0 \sim 200$ provides the best fit of the overall waveform characteristics at INCN (near the west coast of the South Korean Peninsula), a less attenuating path with Q_0 of 300–350 is optimal between NKNTS and TJN.

Discussion

The stochastic nature of the velocity and density perturbations in the underlying crustal and mantle structure allows us to model the statistics of the resulting synthetics, whereas the details of the individual phases and coda depend on the realization of the specific distribution of small-scale heterogeneities. For this reason, an infinite set of ground-motion synthetics can be derived from a given set of von Karman parameters. To estimate the range of ground motions to be expected from the possible realizations associated with the statistical distributions generated in this study, Figure 12 (INCN) and Ⓔ Figure S11 (TJN) compare synthetics for five realizations of the same gradient model of small-scale heterogeneities (models 16–20, Table 1). As expected, the general characteristics, including arrival times and amplitude of the simulated waveforms discussed in this article, persist among the realizations. For example, the variation of the peak amplitude among the five realizations is less than 65%. It is interesting to note, however, that the amplitude of the individual phases can vary by a much larger amount. This result suggests that it is necessary to use an ensemble of simulations generated from different realizations of von Karman distributions of small-scale heterogeneities, in particular for applications depending specifically on P and S amplitudes, such as source discrimination.

Baker *et al.* (2012) reviewed the various mechanisms published for generating S-wave energy from shallow explosions in relatively high-velocity crust (such as the crust between the NKNTS and INCN and TJN). This review concluded that the majority of the S-wave energy is generated by the nonspherical component of the source volume, as opposed to regional scattering. Thus, the findings by Baker *et al.* (2012) are not necessarily at odds with ours that used a purely isotropic source. Pitarka *et al.* (2015) used 0–10 Hz

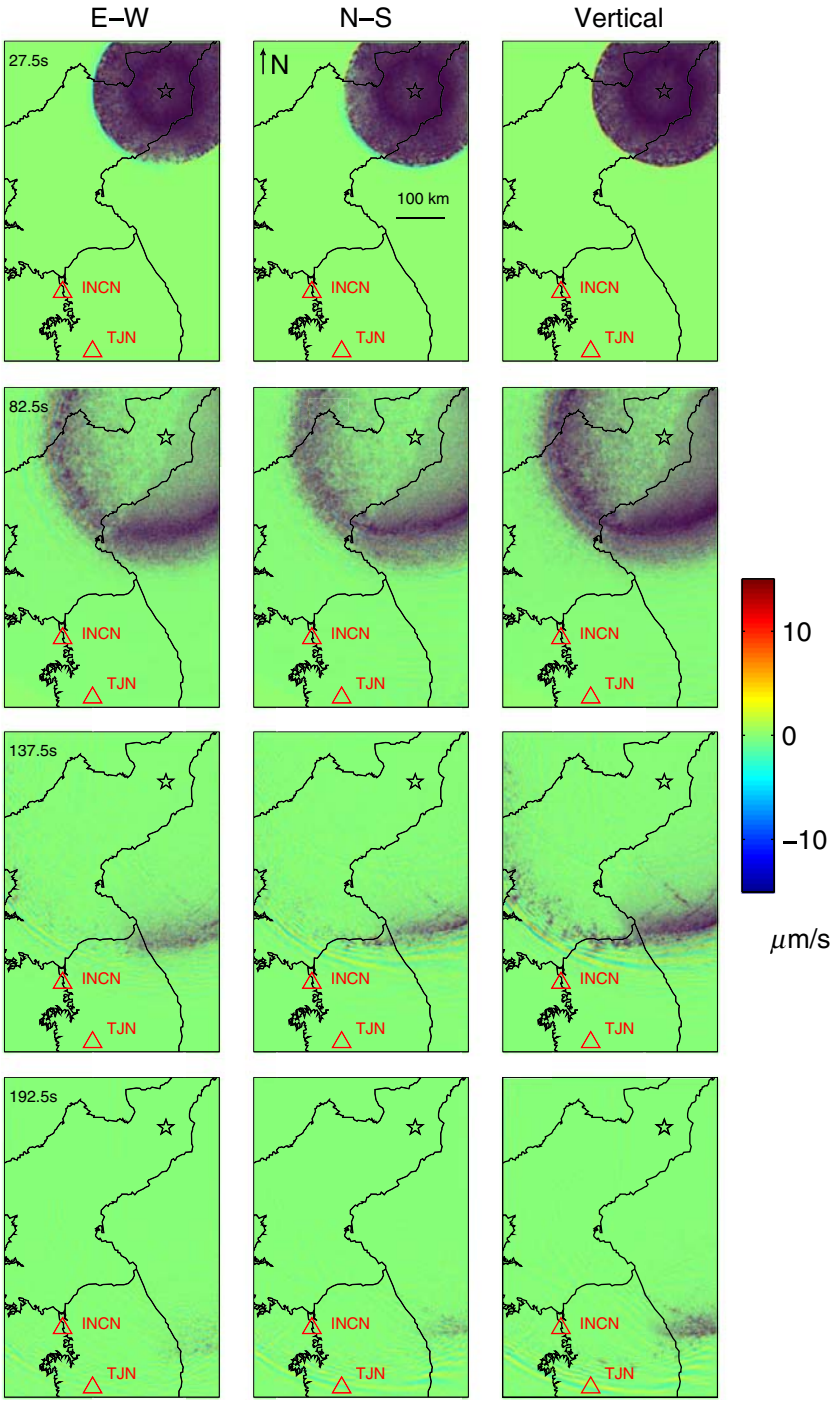

Figure 10. Snapshots of wave propagation for model 6 (Table 1). The color version of this figure is available only in the electronic edition.

numerical simulations and data from the Source Physics Experiment at the Nevada National Security Site to analyze the generation of *S*-wave energy at very near-source distances (< 1 km). They found that a large part of the *S*-wave energy present in the simulations were generated by the source, whereas some scattering off of topography and shallow crustal heterogeneity was required to match the observations. Reasons for the different findings by Pitarka *et al.* (2015) on the importance of very near-source scattering may include the different bandwidths studies (0–10 vs. 0–4 Hz here) and details of the near-source crustal model (grid spacing of 4 m with a minimum V_S of 550 m/s vs. 100 m and 2500 m/s, respectively, in our study). Moreover, it should be noted that our fit between the synthetics and data, such as on the transverse component, has ample room for improvements, with delayed arrival of the largest phase at ~140 s and overprediction of the later-arriving energy at ~140–180 s. Although we show that the contribution from crustal and mantle scattering to the transverse-component energy arriving at regional distance can be significant, further simulations, including effects such as topographic scattering, nonisotropic sources, and nonlinearity, are clearly needed to illuminate the generation of near-source *S*-wave generation.

Topographic scattering was omitted in the simulations carried out in our study and thus was not necessary to obtain the waveform fits presented here. However, Rodgers *et al.* (2010) found that topographic scattering can have significant effects on the resulting wavefield, including enhancement of energy propagation near the source, surface-wave amplification, and *SV*- and *SH*-wave polarization simulated for 0–8 Hz wave propagation from the 2006 and 2009 NKNTs. Their simulations using different proposed locations of the sources a few kilometers apart generated significantly different wavefields, due to the variation-specific source coupling with local topography. Unfortunately, no observations were available within their 40 km × 40 km region for comparison. The largest topographic scattering effects were generated for frequencies higher than the 4 Hz used in our study. On the other hand, Takemura *et al.* (2015) used 3D 0–4 Hz FD simulations, including both surface topography and small-scale heterogeneities to distances of 80 km from explosive and earthquake sources. They found, in general agreement with our results, that the primary source of scattered energy was small-scale heterogeneities in the crust, whereas the cumulative effect of surface topography is limited over long distances. Future studies should further delineate the relative contributions of small-scale heterogeneities and surface topography on seismic waveforms for regional propagation distances.

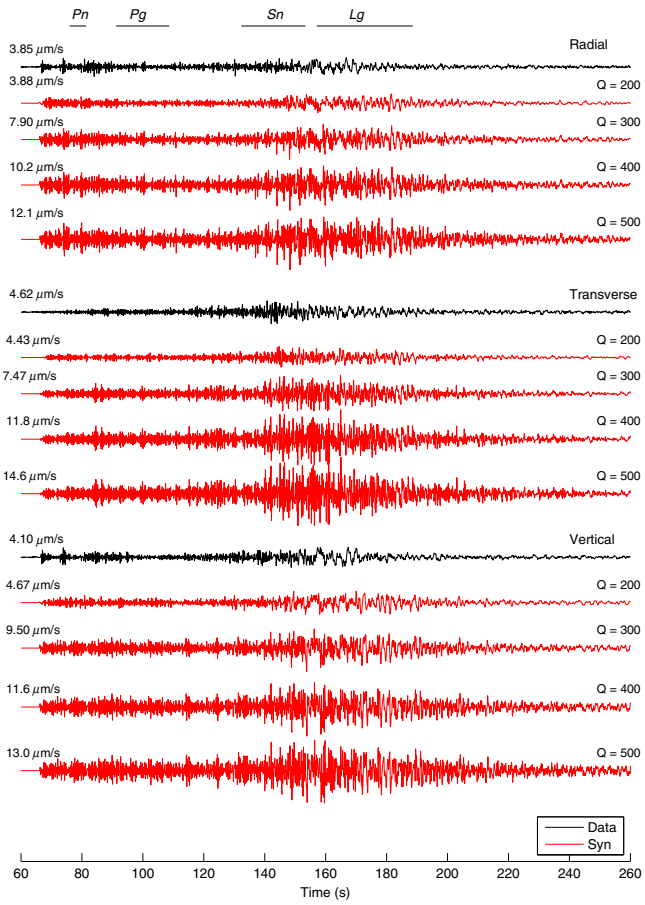

Figure 11. Comparison of data with synthetics generated from models 6 and 6b–d (Table 1) at INCN (effects of different Q_0). The color version of this figure is available only in the electronic edition.

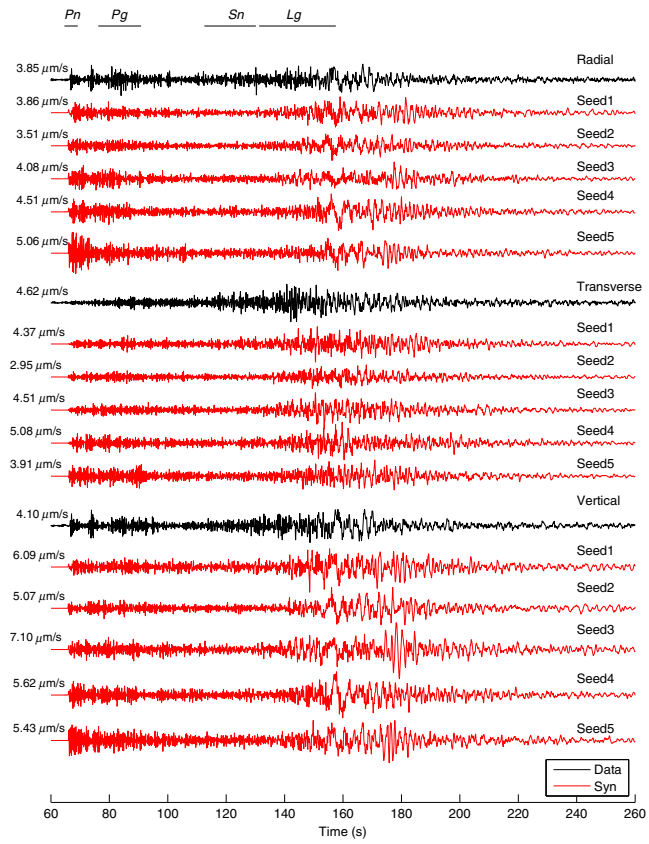

Figure 12. Comparison of data with synthetics generated from a five-realization ensemble of statistical models of small-scale heterogeneities with different seed numbers at INCN. All simulations use the $Q(f)$, a, H/V, and σ of models 16–20 (Table 1). The color version of this figure is available only in the electronic edition.

We found that a vertical correlation length of 1000 m represented an optimal value based on trial-and-error tests within 150–3000 m range. Our preferred value of $a = 1000$ m is longer than that estimated from sonic logs by Plesch *et al.* (2014) and Savran and Olsen (2016) (< 150 m). However, the efficacy of the longer correlation length in reproducing the INCN and TJN waveforms is not too surprising, because the detailed sonic logs with sample spacings < 1 m may be biased toward smaller (high-frequency) correlation lengths, and the rather smooth SALSA3D is deficient in most length scales less than ~10 km or more.

Another possible mechanism, as opposed to the small-scale heterogeneities described above, to improve the characteristics of the synthetics to better match the data is a heterogeneous crust with large-scale blocks generated by local tectonics. Because such a 3D velocity model is not currently available, we tested this hypothesis by a simulation with small-scale heterogeneities, including a larger H/V ratio (20, with a vertical correlation length of 5 km, model 21 in Table 1), as shown in Ⓔ Figure S13. The resulting waveforms at INCN (Ⓔ Fig. S14) reduce the amplitude of the vertical-component Rayleigh wave to about twice that of the data but fail to increase the coda level to realistic levels. Although more tests are needed, this result suggests that a refined crustal model including large-scale basins or blocks, when available, would likely contribute to improving the fit of the synthetic seismograms to the data. Moreover, including such a refined large-scale crustal model may cause a trade-off with respect to the standard deviation of the small-scale perturbations modeled in this study.

To reach a maximum frequency of 4 Hz for the simulations in this study (with a minimum of 6.25 points per minimum S-wave length), we limited the minimum V_S in the crustal models to 2500 m/s. This artificial constraint is implemented at a grid point by resetting V_S to 2500 m/s and replacing V_P by 2500 m/s times the V_P/V_S ratio at the grid point. This modification has little effect on the model within the N-S-oriented band within the Korean Peninsula where $V_S^{\min}$ is already near 3100 m/s (see Ⓔ Fig. S12), in the general path between the NKNTS and western South Korea. However, the ~2 s early arrival time of the Rayleigh wave (e.g., ~150–155 s at INCN in Fig. 12) in the simulations may be caused by discarding the lower near-surface velocities. Moreover, the upper ~3.1 km of the continental shelf in the

Sea of Japan has a V_S as low as 1000 m/s in SALSA3D and may need to be included when modeling data further east.

The accuracy of the attenuation and scattering parameters on the Korean Peninsula estimated in this study relies on an estimate of the magnitude of the 2009 NKNTS explosion. We estimated the moment of our isotropic source function by comparing the low-frequency spectral amplitude for synthetics and data at INCN and TJN (1.58×10^{15} N·m, M_w 4.1). This estimate of the source magnitude is in agreement with Ford *et al.* (2009), supporting our results. A slightly refined estimate of the source magnitude obtained using additional data constraints is not expected to significantly change the conclusions of this study.

Our results demonstrate that state-of-the-art high-frequency 3D wave propagation simulations using high-performance computing can reproduce the general character of records for stations located hundreds of kilometers from the source. We recommend that future work continue to take advantage of these computing capabilities to refine the estimates of the parameters for Q(f) and (small-scale) heterogeneities with systematic inversion methods, rather than trial-and-error modeling, to further minimize any bias from interdependency between modeling parameters. The results of the simulations, in which synthetics are available on a regular grid at the surface, provide a magnificent dataset to test methods for discriminating explosive and earthquake sources as a function of distance from the source and azimuth. Such analysis is currently ongoing.

Conclusions

Recent advances in high-performance computing have facilitated fully deterministic 3D elastodynamic simulations of regional wave propagation (400+ km). We demonstrate these capabilities by modeling time histories for the 2009 North Korea nuclear explosion recorded at stations INCN and TJN in South Korea for frequencies up to 4 Hz in the Sandia/Los Alamos National Laboratory SALSA3D velocity model. Comparison of the synthetics and data show that the SALSA3D model fails to reproduce the main characteristics of the data for this bandwidth. In particular, the synthetics grossly overpredict Rayleigh-wave amplitudes and underpredict the amplitudes of the coda. On the other hand, the addition to SALSA3D of small-scale perturbations of the P and S velocities and densities following a von Karman distribution with correlation lengths of ~1000 m, a Hurst number of 0.1, and an H/V anisotropy of ~5 improves the fit considerably. The results show that the wave propagation along the 400+ km path from the 2009 NKNTS to INCN and TJN is strongly sensitive to the parameters of the small-scale crustal and mantle heterogeneities, as well as to the frequency-dependent attenuation.

Our simulations show a strong depth dependency of the strength of the small-scale heterogeneities on the signature of the synthetics simulated at INCN and TJN from the NKNTS with constraints from data. In particular, models with a gradient in the strength of the velocity and density perturbations and strong scattering (10%) limited to the top 7.5–10 km of the crust tend to provide the synthetics with the best fit to data. Scattering contributions from deeper parts of the crust and mantle are shown to generate *Pn* and *Pg* amplitudes much below those for the data at the two stations. Specifically, the amplitude at the onset of the *Pn* phase can be significantly affected, even for a standard deviation as low as 2% of the small-scale velocity and density perturbations, with respect to the background SALSA3D variation in the lower crust and upper mantle. This result is important for methods used to discriminate between explosive and earthquake sources based on the amplitudes of P and S waves. In addition, the best fits are obtained for an H/V anisotropy of the small-scale heterogeneities of about 5. Larger scale structure (here simulated by heterogeneities with a correlation length of 5 km and an anisotropy factor of 20) may also contribute to the reduction of an otherwise much-too-large amplitude Rayleigh wave.

We used trial-and-error modeling with a constant Q below a threshold frequency (1 Hz) and a frequency-dependent Q following a power law for higher frequencies to constrain the anelastic attenuation parameters on the Korean Peninsula. The results show that constant Q of 200 (INCN) to 350 (TJN) below 1 Hz and a power-law exponent of ~0.3 for both P and S waves generate synthetics in best agreement with the data.

The results of simulations for which the small-scale heterogeneities are omitted in the close vicinity of the source indicate that a little scattering from the near-source area accumulates over the regional path. Our study suggests that the majority of the seismic energy recorded on the transverse component of the recorded waveforms is generated by P–S wave scattering, primarily in the upper crust along the 400+ km path from the source to the stations.

Data and Resources

We use a graphic processing units (GPU)-enabled fourth-order accurate staggered-grid finite-difference (FD) method (AWP-ODC-GPU, Cui *et al.*, 2013), open-source referenced (BSD-2) for our North Korea nuclear test site (NKNTS) wave propagation simulations. Wave propagation of 350 s in the 24 billion grid model using 2500 GPUs required 80–100 min of wall-clock time on the Oak Ridge National Laboratory (ORNL) Titan supercomputer. The CRUST 2.0 model used in SAndia LoS Alamos 3D (SALSA3D) is available at http://igppweb.ucsd.edu/~gabi/crust2.html (last accessed July 2017). The INCN (net IU) and TJN (net KG) records from the 2009 NKNTs were downloaded from Incorporated Research Institutions for Seismology (IRIS).

Acknowledgments

This work was supported by the U.S. Air Force Research Laboratory under Contract Number 16C0017. The simulations were carried out on the Oak Ridge National Laboratory (ORNL) Titan supercomputer. The authors thank two anonymous reviewers for their comments, leading to a better article. The authors are grateful to Te-Yang Yeh for figure contributions.

References

Baker, G. E., J. L. Stevens, and H. Xu (2012). Explosion shear-wave generation in high-velocity source media, *Bull. Seismol. Soc. Am.* **102,** no. 4, 1301–1319, doi: 10.1785/0120110119.

Ballard, S., J. R. Hipp, M. L. Begnaud, C. J. Young, A. V. Encarnacao, E. P. Chael, and W. S. Phillips (2016). SALSA3D: A tomographic model of compressional wave slowness in the Earth's mantle for improved travel-time prediction and travel-time prediction uncertainty, *Bull. Seismol. Soc. Am.* **106,** no. 6, 2900–2916, doi: 10.1785/0120150271.

Bielak, J., R. W. Graves, K. B. Olsen, R. Taborda, L. Ramirez-Guzman, S. M. Day, G. P. Ely, D. Roten, T. H. Jordan, P. J. Maechling, *et al.* (2010). The ShakeOut earthquake scenario: Verification of three simulation sets, *Geophys. J. Int.* **180,** 375–404, doi: 10.1111/j.1365-246X.2009.04417.x.

Birch, F. (1961). The velocity of compressional waves in rocks to 10 kilobars. Part 2, *J. Geophys. Res.* **66,** no. 7, 2199–2224.

Cui, Y., K. Olsen, T. Jordan, K. Lee, J. Zhou, P. Small, D. Roten, G. Ely, D. Panda, A. Chourasia, *et al.* (2010). Scalable earthquake simulation on petascale supercomputers, *Proc. Supercomputing Conference*, New Orleans, Louisiana, 13–19 November 2010.

Cui, Y., E. Poyraz, K. B. Olsen, J. Zhou, K. Withers, S. Callaghan, J. Larkin, C. Guest, D. Choi, A. Chourasia, *et al.* (2013). Physics-based seismic hazard analysis on petascale heterogeneous supercomputers, *International Conference for High-Performance Computing, Networking, Storage and Analysis*, Denver, Colorado, 17–21 December 2013.

Day, S. M., R. W. Graves, J. Bielak, D. Dreger, S. Larsen, K. B. Olsen, A. Pitarka, and L. Ramirez-Guzman (2008). Model for basin effects on long-period response spectra in southern California, *Earthq. Spectra* **24,** 257–277.

De, G. S., D. F. Winterstein, and M. A. Meadows (1994). Comparison of P- and S-wave velocities and *Q*'s from VSP and sonic log data, *Geophysics* **59,** no. 10, 1512–1529.

Dolan, S., C. Bean, and B. Riollet (1998). The broad-band fractal nature of heterogeneity in the upper crust from petrophysical logs, *Geophys. J. Int.* **132,** no. 3, 489–507.

Ford, S. R., D. S. Dreger, and W. R. Walter (2009). Source analysis of the Memorial Day explosion, Kimchaek, North Korea, *Geophys. Res. Lett.* **36,** L21304, doi: 10.1029/2009GL040003.

Ford, S. R., W. S. Phillips, W. R. Walter, M. E. Pasyanos, K. Mayeda, and D. S. Dreger (2010). Attenuation tomography of the Yellow Sea/Korean Peninsula from coda-source normalized and direct Lg amplitudes, *Pure Appl. Geophys.* **167,** 1163–1170, doi: 10.1007/s00024-009-0023-2.

Frankel, A., and R. W. Clayton (1986). Finite difference simulations of seismic scattering: Implications for the propagation of short-period seismic waves in the crust and models of crustal heterogeneity, *J. Geophys. Res.* **91,** no. B6, 6465–6489.

Hartzell, S., S. Harmsen, and A. Frankel (2010). Effects of 3D random correlated velocity perturbations on predicted ground motions, *Bull. Seismol. Soc. Am.* **100,** no. 4, 1415–1426.

Holliger, K. (1996). Upper-crustal seismic velocity heterogeneity as derived from a variety of P-wave sonic logs, *Geophys. J. Int.* **125,** no. 3, 813–829.

Holliger, K. (1997). Seismic scattering in the upper crystalline crust based on evidence from sonic logs, *Geophys. J. Int.* **128,** no. 1, 65–72.

Holliger, K., and A. R. Levander (1992). A stochastic view of lower crustal fabric based on evidence from the Ivrea zone, *Geophys. Res. Lett.* **19,** no. 11, 1153–1156.

Hong, T.-K., and J. Rhie (2009). Regional source scaling of the 9 October 2006 underground nuclear explosion in North Korea, *Bull. Seismol. Soc. Am.* **99,** no. 4, 2523–2540.

Imperatori, W., and P. M. Mai (2013). Broad-band near-field ground motion simulations in 3-dimensional scattering media, *Geophys. J. Int.* **192,** no. 2, 725–744.

Laske, G., and T. G. Masters (1997). A global digital map of sediment thickness, *Eos Trans. AGU* **78,** (Fall Meet.) F483.

Lekic, V., J. Matas, M. Panning, and B. Romanowicz (2009). Measurement and implications of frequency dependence of attenuation, *Earth Planet. Sci. Lett.* **282,** 285–293.

Levander, A. R., R. W. England, S. K. Smith, R. W. Hobbs, J. A. Goff, and K. Holliger (1994). Stochastic characterization and seismic response of upper and middle crustal rocks based on the Lewisian Gneiss Complex, Scotland, *Geophys. J. Int.* **119,** no. 1, 243–259.

McNamara, D., M. Meremonte, J. Z. Maharrey, S.-L. Mildore, J. R. Altidore, D. Anglade, S. E. Hough, D. Given, H. Benz, L. Gee, *et al.* (2012). Frequency-dependent seismic attenuation within the Hispaniola Island region of the Caribbean Sea, *Bull. Seismol. Soc. Am.* **102,** 773–782, ISSN: 0037-1106.

Mitchell, B. J., Y. Pan, J. Xie, and L. Cong (1997). *Lg* coda *Q* variation across Eurasia and its relation to crustal evolution, *J. Geophys. Res.* **102,** no. B10, 22,767–22,779.

Nafe, J. E., and C. L. Drake (1960). Physical properties of marine sediments, in *The Sea*, M. N. Hill (Editor), Vol. 3, Interscience, New York, New York, 794–815.

Nakata, N., and G. Beroza (2015). Stochastic characterization of mesoscale seismic velocity heterogeneity in Long Beach, California, *Geophys. J. Int.* **203,** 2049–2054.

Olsen, K. B. (1994). Simulation of three-dimensional wave propagation in the Salt Lake Basin, *Ph.D. Thesis*, University of Utah, Salt Lake City, Utah, 157 p.

Olsen, K. B. (2000). Site amplification in the Los Angeles basin from 3D modeling of ground motion, *Bull. Seismol. Soc. Am.* **90,** S77–S94.

Olsen, K. B., and B. H. Jacobsen (2011). Spatial variability of ground motion amplification from low-velocity sediments including fractal inhomogeneities with special reference to the Southern California basins, *Proc. 4th IASPEI/IAEE International Symposium Effects of Surface Geology on Seismic Motion (ESG4)*, University of California at Santa Barbara, California, 23–26 August 2011.

Pasyanos, M. E., W. R. Walter, M. P. Flanagan, P. Goldstein, and J. Bhattacharyya (2004). Building and testing an a priori geophysical model for western Eurasia and North Africa, *Pure Appl. Geophys.* **161,** 235–281.

Patton, H. J., and F. V. Pabian (2014). Comment on "Advanced seismic analysis of the source characteristics of the 2006 and 2009 North Korean nuclear tests, by J.R. Murphy, J.L. Stevens, B.C. Kohl, and T.J. Bennett", *Bull. Seismol. Soc. Am.* **104,** no. 4, 2104–2110.

Phillips, W. S., K. M. Mayeda, and L. Malagnini (2014). How to invert multi-band, regional phase amplitudes for 2-D attenuation and source parameters: Tests using the USArray, *Pure Appl. Geophys.* **171,** 469–484.

Pitarka, A., R. J. Mellors, W. R. Walter, S. Ezzedine, O. Vorobiev, T. Antoun, J. L. Wagoner, E. M. Matzel, S. R. Ford, A. J. Rodgers, *et al.* (2015). Analysis of ground motion from an underground chemical explosion, *Bull. Seismol. Soc. Am.* **105,** no. 5, 2390–2410, doi: 10.1785/0120150066.

Plesch, A., J. H. Shaw, X. Song, and T. H. Jordan (2014). Stochastic descriptions of fine-scale basin velocity structure from well logs and the SCEC Community Velocity Model (CVMH), *Seismol. Res. Lett.* **85,** no. 2, 382.

Raoof, M., R. Herrmann, and L. Malagnini (1999). Attenuation and excitation of three-component ground motion in southern California, *Bull. Seismol. Soc. Am.* **89,** 888–902.

Rodgers, A., N. A. Petersson, and B. Sjogreen (2010). Simulation of topographic effects on seismic waves from shallow explosions near the North Korean nuclear test site with emphasis on shear wave generation, *J. Geophys. Res.* **115,** no. B11, doi: 10.1029/2010JB007707.

Savran, W. H., and K. B. Olsen (2016). Model for small-scale crustal heterogeneity in Los Angeles basin based on inversion of sonic log data, *Geophys. Res. Lett.* **205,** 856–863.

Shin, J. S., D.-H. Sheen, and G. Kim (2010). Regional observations of the second North Korean test on 2009 May 25, *Geophys. J. Int.* **180,** 243–250.

Steck, L. K., C. A. Rowe, M. L. Begnaud, W. S. Phillips, V. L. Gee, and A. A. Velasco (2004). Advancing seismic event location through difference constraints and three-dimensional models, *Proc. of the 26th*

Seismic Research Review—Trends in Nuclear Explosion Monitoring, Orlando, Florida, 346–355.

Takemura, S., T. Furumura, and T. Maeda (2015). Scattering of high-frequency seismic waves caused by irregular surface topography and small-scale velocity inhomogeneity, *Geophys. J. Int.* **201,** 459–474.

Tatarski, V. I. (1961). *Wave Propagation in a Turbulent Medium*, McGraw-Hill, New York, New York.

Wagner, G. S. (1996). Numerical simulations of wave propagation in heterogeneous wave guides with implications for regional wave propagation and the nature of lithospheric heterogeneity, *Bull. Seismol. Soc. Am.* **86,** 1200–1206.

Wagner, G. S., and C. A. Langston (1992). A numerical investigation of scattering effects for teleseismic plane wave propagation in a heterogeneous layer over a homogeneous half-space, *Geophys. J. Int.* **110,** no. 3, 486–500, doi: 10.1111/j.1365-246X.1992.tb02087.x.

Wang, N., Y. Shen, A. Flinders, and W. Zhang (2016). Accurate source location from waves scattered by surface topography, *J. Geophys. Res.* **121,** no. 6, 4538–4552, doi: 10.1002/2016JB012814.

Withers, K. B., K. B. Olsen, and S. M. Day (2015). Memory-efficient simulation of frequency-dependent *Q*, *Bull. Seismol. Soc. Am.* **105,** 3129–3142, doi: 10.1785/0120150020.

Wu, R. S., Z. Xu, and X.-P. Li (1994). Heterogeneity spectrum and scale-anisotropy in the upper crust revealed by the German Continental Deep-Drilling (KTB) Holes, *Geophys. Res. Lett.* **21,** no. 10, 911–914.

Xie, J., Z. Wu, R. Liu, D. Schaff, Y. Liu, and J. Liang (2006). Tomographic regionalization of crustal *Lg Q* in eastern Eurasia, *Geophys. Res. Lett.* **33,** L03315, 1–4.

Department of Geological Sciences, GMCS 231A
San Diego State University
San Diego, California 92182
kbolsen@mail.sdsu.edu
(K.B.O.)

Los Alamos National Laboratories
Los Alamos, New Mexico 87545
(M.B., S.P.)

Department of Geoscience
Aarhus University
Høegh-Guldbergs Gade 2, Building 1671, 214
8000 Aarhus C, Denmark
(B.H.J.)

Manuscript received 13 July 2017;
Published Online 20 March 2018